# Aerodynamic performance of a flyable flapping wing rotor with dragonfly-like flexible wings

Y. Pan *, S. Guo, J. Whidborne, X. Huang

*Centre for Aeronautics, School of Aerospace, Transport and Manufacturing, Cranfield University, Bedford, UK*

## ARTICLE INFO

## ABSTRACT

Drawing inspiration from insect flapping wings, a Flapping Wing Rotor (FWR) has been developed for Micro Aerial Vehicle (MAV) applications. The FWR features unique active flapping and passive rotary kinematics of motion to achieve a high lift coefficient and flight efficiency. This study thoroughly investigates the aerodynamic performance and design of a bio-inspired flexible wing for FWR-MAVs, emphasizing its novel backward-curved wingtip and variable spanwise stiffness resembling a dragonfly's wing. The research departs from previous aerodynamic studies of FWR, which focused predominantly on rectangular and rigid wings, and delves into wing flexibility. Employing Computational Fluid Dynamics (CFD), Computational Structural Dynamics (CSD), and experimental measurements, the study demonstrates the aerodynamic benefits of the dragonfly-inspired FWR wingtip shape and its reinforced structure. Fluid-Structure Interaction (FSI) analysis is used to examine the effects of elastic deformation encompassing twist and bending on aerodynamic forces. The results underscore the importance of bending deformation in enhancing lift and power efficiency and propose a method for analysing variable stiffness along the wingspan using a vortex delay mechanism that is induced by delayed flapping motion. By comparing modelled and measured stiffness, the study validates the flexibility of the FWR wing, revealing optimal aerodynamic efficiency is achieved through moderate flexibility and spanwise stiffness variation. The curving leading-edge beam forming the sweep-back wingtip offers a practical approach to obtaining variable stiffness and aerodynamic benefits for FWR-MAVs. Using the same pair of dragonfly-like flexible wings, FWR-MAVs have effectively exhibited VTOL and hovering flight capabilities, spanning from a 25-g single-motor drive model to a 51-g dual-motor drive model. This research provides valuable insights into flexible wing design for FWR-MAVs, leveraging biomimicry to improve flight efficiency.

## 1. Introduction

Biomimetic micro air vehicles inspired by the flapping flight of insects have attracted a lot of attention in recent years. Many Flapping Wing Micro Aerial Vehicles (FW-MAVs) have been extensively developed, however due to the characteristics of low Re flight, the existing vehicles still have limitations in terms of lift generation and power efficiency [1–3]. To date, studies on a novel flapping wing rotor (FWR), which combines active flapping and passive rotation motions of the asymmetrically installed wings, have grown in importance as a way of improving the aerodynamic performance of FW-MAVs [4,5]. The evidence presented in previous research suggests that at the same level of power efficiency, the lift produced by the FWR wing can be twice as high as the lift produced by a rotary wing [4]; the aerodynamic efficiency of the FWR wing is much higher than the typical insect-inspired

flapping wings [6,7]. Nevertheless, when examining earlier FWR-MAV designs, the wings predominantly adopted a simple rectangular plate, rather than a bio-inspired configuration. This trend persists in recent flyable models, with Chen et al. [8] still employing rectangular planes. Dong's FWRs from 2022 [9] used a semi-elliptical shape with a rigid linear leading edge beam, a departure from wings that closely mimic biological designs, such as those of dragonflies. Though Wang et al. [10] provided an analysis on geometric parameters like aspect ratio and the second area moment's effects on FWR wings, their study centred around rigid plates. Recent literature still presents a noticeable gap in comprehensive studies addressing the influence of bionic wing shape and flexibility on aerodynamics within FWR-MAVs.

The insect wing, unlike the wing of a bird, lacks muscles and is therefore subject to passive deformation, which primarily is composed of transient spanwise bending, twist, and chordwise camber variation.

## Nomenclature

| | | | |
|---|---|---|---|
| MAV | Micro Aerial Vehicle | $\Delta t_r$ | Non-dimensional reversal time interval |
| FWR | Flapping-Wing Rotor | $t_n$ | Non-dimensional delayed flapping time |
| FW | Flapping-Wing | $C_l, C_d, C_m$ | Lift, drag, and rotational moment coefficients |
| CFD | Computational Fluid Dynamics | $\bar{C}_l, \bar{C}_d, \bar{C}_m$ | The average lift, drag, and rotational moment coefficients |
| CSD | Computational Structural Dynamics | | |
| FSI | Fluid-Structure Interaction | $L$ | The average lift |
| LE-beam | Leading Edge beam | $P$ | Power input |
| $R, c$ | Semi-wingspan, root chord length | $P_f$ | Aerodynamic power efficiency |
| $\lambda$ | Aspect ratio | $S_p$ | Power efficiency |
| $e, e_s$ | Thickness of the LE-beam and wing skin | $E_k, E_p$ | Kinetic energy, Potential energy |
| $d_1, d_2$ | Diameters of the chordwise sub-beams | $q$ | Generalized coordinate |
| $\psi, \phi, \alpha$ | The angle of rotation, flapping, and pitching | $Q$ | Generalized external forces |
| $\dot{\alpha}, f, n$ | Pitching velocity, flapping frequency, rotation speed | $\delta_e$ | Node displacements |
| $U$ | Reference flapping velocity | $K_e$ | Stiffness matrix of the beam element |
| $\Phi$ | Flapping amplitude | $\varepsilon$ | Strain vector of the skin |
| $t, \hat{t}$ | Real time, non-dimensional time | $\upsilon$ | Skin volume |
| $\alpha_u, \alpha_d$ | The geometric angle of attach of the wing at mid-upstroke and mid-downstroke respectively | | |

For conventional flapping wings, wing deformation and flexibility have been extensively studied. The wing deformation is significantly determined by the elastic responses to aerodynamic and inertial forces [11,12]. Proper deformation of the flapping wing can improve aerodynamic performances in terms of lift-to-drag ratio [13], flight efficiency [14], and reducing the energy costs [15]. As the flexibility of a flapping wing has considerable effects on its aerodynamic characteristics [16,17], a moderate stiffness should be adopted in order to achieve high lift and propulsive efficiency [18,19]. Specifically, Heathcote et al. [20] discovered that in a water tunnel study, a degree of spanwise flexibility contributed to a slight increase in thrust coefficient and a slight drop in power requirements, resulting in greater efficiency for Strouhal numbers above 0.2. Similarly, Yang et al. [21] showed in their experimental study that the span stiffness has a significant effect on the lift generation, while the chordwise stiffness has a greater impact on the thrust generation.

The aerodynamic performance of flexible flapping wings is also affected by the wing geometry, including the wing shape and aspect ratios, as well as the wing structure. For example, an increase in aspect ratio and root cut-off can improve the lift production of a flexible flapping wing during hovering flight, as found by a previous study [14]. Nan et al. [22] found that a trapezoidal shape, a straight leading edge, and an aspect ratio of 9.3 can achieve excellent performance for a hummingbird-sized wing. However, a comparative analysis of flapping wings with different shapes has also revealed that high aspect ratio wings, such as those with aspect ratios of 4.5 and 6.0, provide less lift than rigid wings due to lower pitch angles during the mid-stroke [15]. These results indicate that the findings on wing shape and aspect ratio may be restricted to specific case studies and might not be universally applicable to all flapping models, particularly not for FWRs, which exhibit unique kinematics compared to traditional flappers.

Multiple studies have demonstrated that reinforced structures, such as a rigid leading edge, a reinforced trailing edge, a rigid triangle at the wing root, and diagonal battens, can be incorporated into flexible wing designs [15,23,24]. However, most flapping wing structures are assumed to have approximately isotropic homogeneous flexibility [25,26,15] or anisotropic flexibility but uniform torsional or bending stiffness [27,28], and often neglect the effects of wingtip and lump mass in the analysis. In contrast, the current study focuses on a dragonfly-like flexible FWR wing, which features variable stiffness along the wingspan and a curving leading-edge beam that reinforces the wingtip.

Recent studies have highlighted the non-trivial mechanisms governing the aerodynamic performance of flexible wings, including the delayed burst of the leading-edge vortex [24,29,30], and delayed pitch rotation [15]. These effects have been shown to enhance lift production. In this study, we investigate, to our knowledge for the first time, the delayed flapping motion by which wing spanwise flapping deformation governs lift enhancement for an FWR model.

The aerodynamics and structural dynamics of the FWR wing are strongly coupled, resulting in a complex fluid-structure interaction (FSI) problem. To overcome this challenge, a computational FSI analysis, which couples a computational fluid dynamics (CFD) solver and a computational structural dynamics (CSD) solver, is commonly used to provide detailed information on both flow fields and structural dynamics [30,31]. In this study, we first consider a global point of view in which the effect of dragonfly-like shape on the aerodynamic performance of the FWR model is compared with the baseline rectangular shape by CFD and experimental approaches, also taking aspect ratio into account. We also explore the contribution of the reinforced wingtip and inherent wing elastic deformation to the unsteady aerodynamics and power efficiency of the FWR model through FSI analysis and experiments. Furthermore, we address how wing bending deformation significantly affects aerodynamic performance and propose an optimization and generalizable strategy to achieve efficient biomechanics for FWR-MAV by adjusting the stiffness quantity of the wing along the spanwise direction. Through experimentation and flight tests, the dragonfly-inspired flexible wings demonstrated enhanced lift production and power efficiency, effectively supporting the flight capabilities of the FWR model.

## 2. Modelling and methods

### 2.1. Dragonfly-inspired FWR wing model

Several studies of bird and dragonfly wings have revealed that the outer section of the wing has a sweep angle or gradually shrinks along the spanwise direction [19], [32]. The shape of the dragonfly forewing and hindwing exhibits a continuous backward curvature of the wingtip at 80% to 90% of the span [32,33]. The flexible wing for an FWR-MAV taken in this study imitates the shape of a dragonfly's hindwing (Sympetrum sanguineum) [32], as shown in Fig. 1.

The aspect ratio $\lambda$ of the wing refers to the ratio of the semi-span $R$ to the root chord length $c$ in this study, as shown in Fig. 1(b). The dragonfly-like FWR wing shown in Fig. 1(b) has an aspect ratio of $\lambda = 2.67$. The structure of the FWR wing is composed of a carbon/epoxy frame and polyimide film. The carbon fibre beam has a density of $1.49 \times 10^{-3}$ g/mm$^3$ and elastic modulus of 230 GPa. The polyimide film has
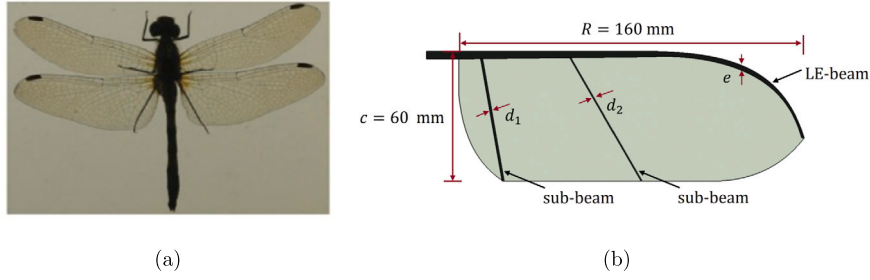
(a)                                        (b)

**Fig. 1.** (a) Wings of Dragonfly (Sympetrum sanguineum) [32]; (b) Structural layout and dimensions of the dragonfly-like FWR wing.
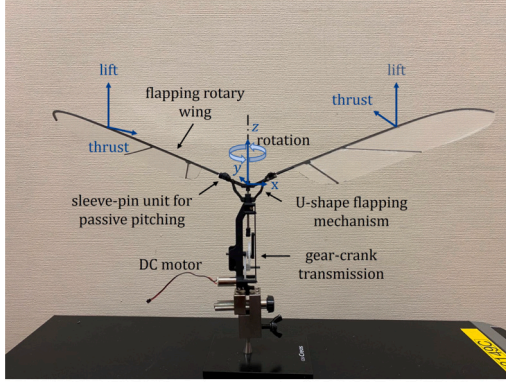


**Fig. 2.** A flyable FWR-MAV.

the following material properties: thickness 0.015 mm, density $1.42 \times 10^{-3}$ g/mm$^3$, and elastic modulus 2.5 GPa. Inspired by the membrane and veins of a dragonfly, which vary along the wingspan and chordwise direction, the thickness $e$ of the Leading Edge beam (LE-beam) of the FWR wing gradually changes from 3.5 mm at the wing root to 1.5 mm at the wingtip. The chordwise sub-beams choose two carbon fibre rods with diameters $d_1 = 1$ mm and $d_2 = 0.6$ mm, respectively.

### 2.2. An FWR-MAV model and the kinematics of motion

A flyable FWR-MAV test model with a pair of dragonfly-like wings is shown in Fig. 2, driven by a DC motor. The main body of the test model has a total height of 103 mm, while the wing's semi-span measures 160 mm. The test model, including a 5 g motor, has a total weight of 16.25 g. The FWR performs a vertical flapping motion ($\phi$) through a gear-crank transmission mechanism. A sleeve-pin unit is mounted at the free end of the U-shape flapping mechanism that connects to the wing root, allowing the wing to perform a passive pitching motion ($\alpha$) within a

range of angular variation. The flapping wings would produce lift and axially symmetric thrust that would result in a passive rotation motion ($\psi$).

Fig. 3(a) shows the coordinate system that can be used to describe the kinematics of the FWR wing. The rigid-body rotations involve four frames: the inertial frame $oxyz$ based on the horizontal plane, two intermediate frames $ox'y'z'$ and $ox''y''z''$, and the wing-fixed frame $ox_wy_wz_w$. The wing would undergo elastic deformation due to the aerodynamic and inertial forces produced by the rigid-body rotations.

For the wing going downstroke at the initial time, the flapping angle is given as

$$\phi = 0.5\Phi\cos\left(2\pi\hat{t}\right) \tag{1}$$

where $\Phi$ is the flapping amplitude; $\hat{t} = ft$ is the dimensionless time ranging from 0 to 1 in a flapping cycle, with the flapping frequency $f$ and physical time $t$.

When the FWR wing performs passive pitching motion, its angle of attack changes abruptly during the flapping stroke reversal, then remains constant in the rest of downstroke and upstroke [8]. According to the reference [4,34], the pitching angle velocity of the wing in the reversal phase at the end of each stroke can be described as

$$\dot{\alpha} = \frac{2f(\alpha_u - \alpha_d)}{\Delta t_r}\left[(-1)^{(2\hat{t}+0.5)} - \cos(\frac{4\pi\hat{t}}{\Delta t_r} - (2\hat{t} - 0.5)\pi)\right] \tag{2}$$

where $\Delta t_r$ indicates the dimensionless pitching time with respect to the flapping period.

In this study, the FWR kinematics of motion is set as follows. The active flapping motion is sinusoidal and symmetric, ranging from -30° to 30°, as shown in Fig. 3(b). The pitching axis $x_w$ of the FWR wing is aligned with the leading edge. The passive wing pitching angle has a minimum -10° during downstroke, i.e., $\alpha_d = -10°$, and a maximum 30° during the upstroke, i.e., $\alpha_u = 30°$. In the numerical analysis, the rotation speed denoted by $n$ is assumed to remain constant over a flapping cycle.



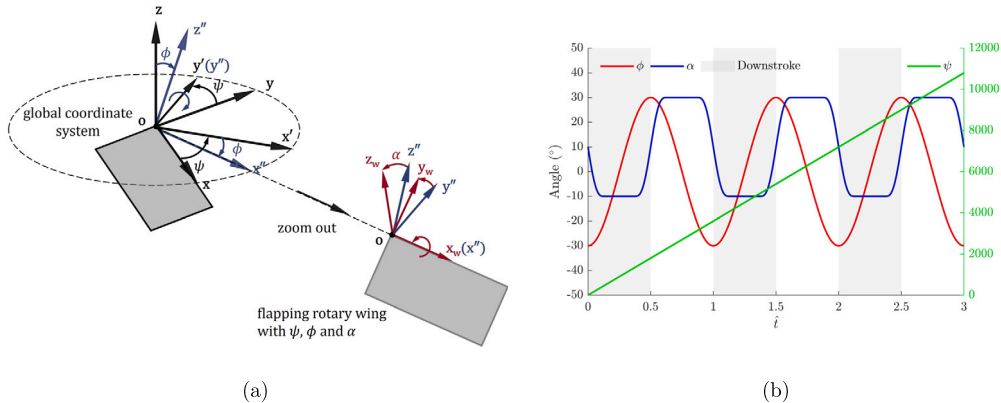(a)                                        (b)

**Fig. 3.** (a) Coordinate system definition for the single FWR wing; (b) Time courses of the sinusoidal flapping, passive pitching and rotation motions. (For interpretation of the colours in the figure(s), the reader is referred to the web version of this article.)
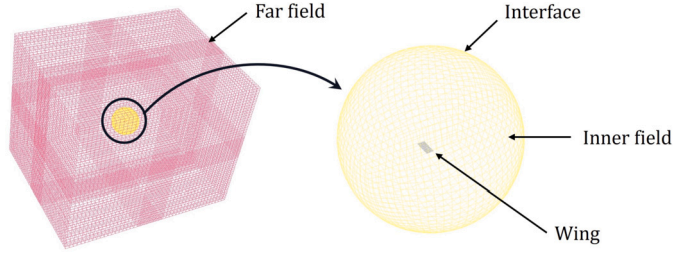
**Fig. 4.** Diagram of the CFD model.

### 2.3. Aerodynamic analysis

The aerodynamic analysis for the whole FWR wing is performed using the computational fluid dynamics (CFD) method, which is governed by the three-dimensional unsteady Navier-Stokes equations. A turbulent model of k-$\omega$ SST within the commercial software Fluent is employed in this study. The three-dimensional CFD model, which is a structured and boundary-fitted O-H type mesh, combines a far field, spherical interfaces, and the FWR wing as shown in Fig. 4. Thus, the fluid field is divided into an outer and an inner fluid field. The inner fluid field moves with the wing rigid rotations by using the dynamic mesh method, and it is compiled with a user-defined functions script that specifies the predefined wing kinematics of motion, as illustrated in Fig. 3(b). The wing is analysed as a rigid body in the CFD simulations. The CFD model is validated by comparing an initial example to experimental data. This will be detailed in the forthcoming Section 3.1.1 and Fig. 9.

The aerodynamic forces produced by the wing in the inertia coordinate system are obtained by integrating the pressure and velocity components in the flow field around the wing at each physic time [35]. The lift, drag, and rotational moment coefficients of the FWR wing are defined as follows:

$$C_l = \frac{l}{0.5\rho \bar{U}^2 S}, \; C_d = \frac{d}{0.5\rho \bar{U}^2 S}, \; C_m = \frac{m}{0.5\rho \bar{U}^2 S \bar{c}} \tag{3}$$

where $l$ is the vertical lift force, $d$ is the horizontal drag force, and $m$ is the rotational moment along the $z$-axis in the inertial system; $\rho$ is the fluid density; $S$ is the wing area; $barc$ is the mean chord length of the wing. The time averaged values of lift, drag, and moment coefficients are donated by $\bar{C}_l$, $\bar{C}_d$, and $\bar{C}_m$. The reference velocity $\bar{U}$ is defined by the average flapping velocity at the wingtip, $\bar{U} = 2f\Phi R$, where $R$ is the spanwise length of the wing.

In the previous study [34], the aerodynamic power efficiency of the FWR wing was denoted by a dimensionless power factor $P_f$ that was the ratio of the mean lift coefficient to the mean aerodynamic power efficiency. As the mean aerodynamic power was calculated by the total power required for the wing to produce forces, the aerodynamic power efficiency $P_f$ is determined by the following equation in this study:

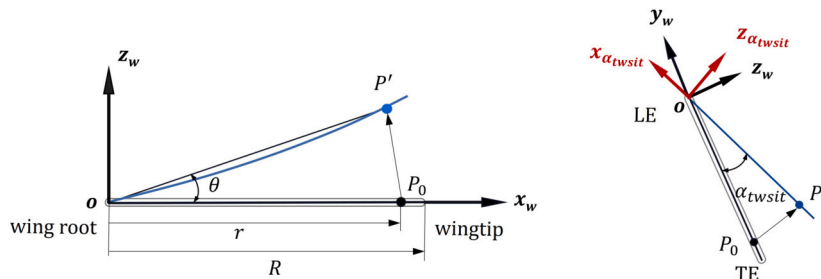$$P_f = \frac{\bar{C}_l}{\bar{C}_l - \bar{C}_d} \tag{4}$$

In experiments, the power efficiency of the FWR model $S_P$ is evaluated by the ratio of the average lift force generated by the wings $L$ (N) over a flapping cycle to the power input $P$ (W) from the motor, i.e.,

$$S_P = \frac{L}{P} \tag{5}$$

### 2.4. Structural analysis of the flexible FWR wing

In addition to the rigid body motion of the FWR as described above, the structural dynamic equation of the flexible FWR wing can be derived from Lagrange's equation as follows:

$$\frac{d}{dt}\left(\frac{\partial E_k}{\partial \dot{q}}\right) - \frac{\partial E_k}{\partial q} + \frac{\partial E_p}{\partial q} = Q \tag{6}$$

where $E_k$ and $E_p$ are the wing's kinetic and potential energy, respectively, and $Q$ denotes the generalized external forces including the drive torque and aerodynamic forces. The generalized coordinate $q$ that describes the wing kinematics is expressed by,

$$q = \left[[q^{rot}]^T, [q^{ela}_{twist}]^T, [q^{ela}_{bend}]^T\right]^T \tag{7}$$

where $q^{rot}$ denotes the generalized coordinates of rigid-body rotations referring to rotating, flapping and pitching angles respectively; $q^{ela}_{twist}$ and $q^{ela}_{bend}$ represent the generalized coordinates of the wing elastic deformation including twisting angle ($\alpha_{twist}$) and bending angle ($\theta$) respectively.

For a general point $P_0$ on the wing, its position vectors in the inertial frame and the wing-fixed frame are respectively expressed as $r_i = [x_i \; y_i \; z_i]^T$ and $r_w = [x_w \; y_w \; z_w]^T$, as shown in Fig. 2 and Fig. 5. The transformation matrix from the wing-fixed frame to the inertial frame is given as $R_{w \to i} = R_\psi R_\phi R_\alpha$ [4]. The kinetic energy of the wing is obtained by,

$$E_k = \frac{1}{2}\iint_s e_s \rho \dot{r}_i^T \dot{r}_i ds \triangleq \frac{1}{2}\dot{q}^T M_w \dot{q} \tag{8}$$

where $e_s$ is the wing skin thickness; s is the area of the undeformed wing; $M_w$ is the wing's mass matrix.

The potential energy $E_p$ is yielded by the elastic energy storage in the deformations of wing skin and the beams, i.e., $E_p = E_p^{skin} + E_p^{beam}$. The potential energy of wing skin is calculated by the nonlinear strain-displacement relations for plate with a moderate deformation [28],

$$E_p^{skin} = \frac{1}{2}\iiint \varepsilon^T C \varepsilon dv \tag{9}$$

where $v$ is the skin volume; $\varepsilon$ is the strain vector of the skin. According to the finite element model, the strain energy for a beam element is given by,

$$(E_p^{beam})_e = \frac{1}{2}(\delta_e)^T K_e \delta_e \tag{10}$$

where $\delta_e$ represents the node displacements; $K_e$ is the stiffness matrix of the beam element. With the stiffness matrix and the boundary conditions, which involve the node displacements at both the wing root and
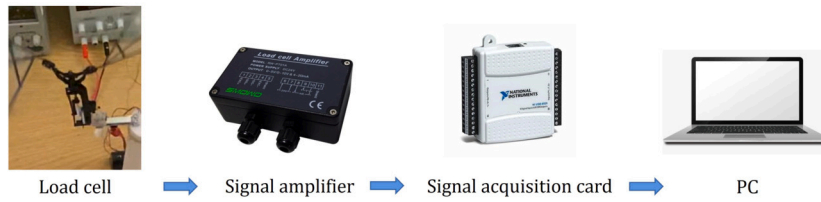


**Fig. 5.** 2D views of bending and twisting deformation of the flexible FWR wing.

Load cell ➡ Signal amplifier ➡ Signal acquisition card ➡ PC

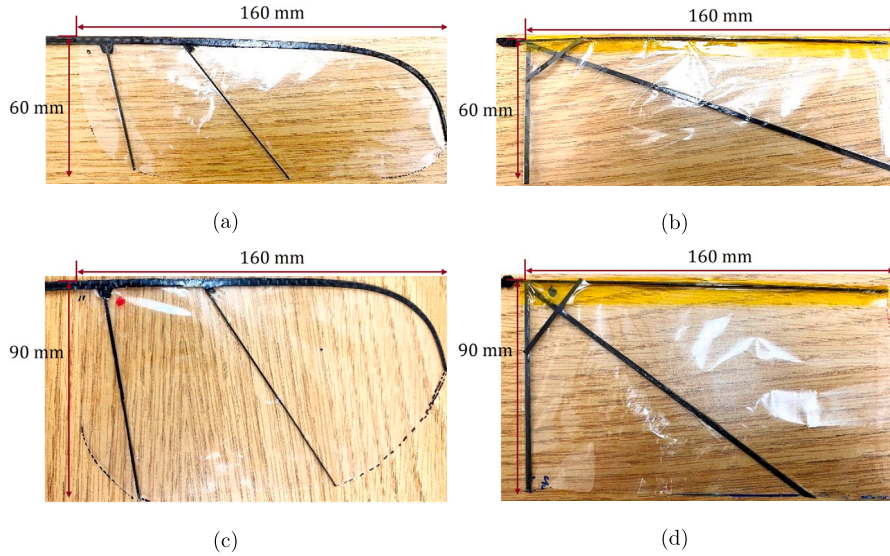**Fig. 6.** 2D views of bending and twisting deflections of the flexible FWR wing.



**Fig. 7.** Wing Structure and dimensions for the FWR model: (a) Wing DW-A and (b) Wing RW-A ($\lambda = 2.67$); (c) Wing DW-B and (d) Wing RW-B ($\lambda = 1.78$).

tip, as governed by the generalized coordinates $q_{twist}^{ela}$ and $q_{bend}^{ela}$, the overall potential energy of the LE-beam $E_p^{beam}$ can be derived.

Therefore, the structural dynamic equation (Eq. (6)) can be rewritten in a discrete form based on the Newmark method for transient structural analysis as follows:

$$\boldsymbol{M}_w \ddot{\boldsymbol{q}}(t) + (\boldsymbol{K}_v(t) + \boldsymbol{K})\boldsymbol{q}(t) = \boldsymbol{Q}_{aero}(t) \qquad (11)$$

where $\boldsymbol{K}$ and $\boldsymbol{K}_v$ are overall static stiffness matrix and dynamic stiffness matrix respectively; $\boldsymbol{Q}_{aero}$ is composed of aerodynamic forces and the initial forces related to the accelerations of wing motions.

The FWR wing kinematics of motion introduced in Section 2.2 are applied to the wing base as boundary conditions in the transient structural analysis, which is completed by the CSD solver Transient Structural. Therefore, the numerical simulation for FSI is conducted as follows: Initially, the unsteady aerodynamic forces produced by the wing motion at the instant $t$ are computed in CFD. Secondly, the aerodynamic forces are transferred from the aerodynamic grid to the structural grid, and the wing deformation is calculated by solving the structural dynamic equation at the instant $t$ in CSD. After the deformation value converges, the displacement of the structural grid is then translated to the aerodynamic grid to update the shape of the flexible wing, which returns to the aerodynamic calculation at the next time step, and so on iteratively.

### 2.5. Experiment of the FWR-MAV test model

An experimental platform comprising the devices depicted in Fig. 6 was constructed to measure the instantaneous force produced by the FWR wings. The FWR was operated by a DC motor supplied by a DC supply and placed on a load cell (with a capacity of 200 g and an accuracy of 0.05 percent F.S.). The voltage signal from the load cell was transmitted to the data acquisition device through a 1K-gain signal amplifier (NI USB-6009). The data were then transmitted to the Lab-

**Table 1**
Dimensions and weight of wings.

| Wing Name | Wing DW-A | Wing DW-B | Wing RW-A | Wing RW-B |
|---|---|---|---|---|
| Dimension (mm) | 160×60 | 160×90 | 160×60 | 160×90 |
| $\lambda$ | 2.67 | 1.78 | 2.67 | 1.78 |
| Weight (g) | 1.21 | 1.35 | 0.81 | 0.96 |

VIEW programme on the PC to quantify the lift force, filtered using the 2nd-order low-pass Chebyshev algorithm with the low-pass cut-off frequency set to five times the flapping frequency of the FWR model [36,37]. This force measurement method was utilised and validated in previous works [8,38].

### 3. Results and discussion

#### 3.1. Effect of wingtip shape

##### 3.1.1. Aerodynamic forces and power efficiency

The most remarkable characteristic of a dragonfly's wing is the gradual backward curvature of the LE near the wingtip. We first investigate the aerodynamic forces and power efficiency of the dragonfly-like wings and the baseline rectangular wings with the same aspect ratio. The two types of physical wings are installed on the FWR-MAV model, as shown in Fig. 7, and their dimensions and weights are listed in Table 1. The first group of test is the dragonfly-like wing DW-A and its baseline rectangular wing RW-A with the same aspect ratio of $\lambda = 2.67$. In the second group containing the dragonfly-like wing DW-B and its base wing RW-B, the chord length is extended and the aspect ratio is $\lambda = 1.78$.

The experimental findings demonstrated that aerodynamic performance is greatly enhanced when the FWR wing adopts the sweep-back shape of the wingtip. In general, for the same input power and flapping frequency, the DW wings consistently produced a higher lift force than their corresponding base wings (Fig. 8(a)(b)), which can be attributed
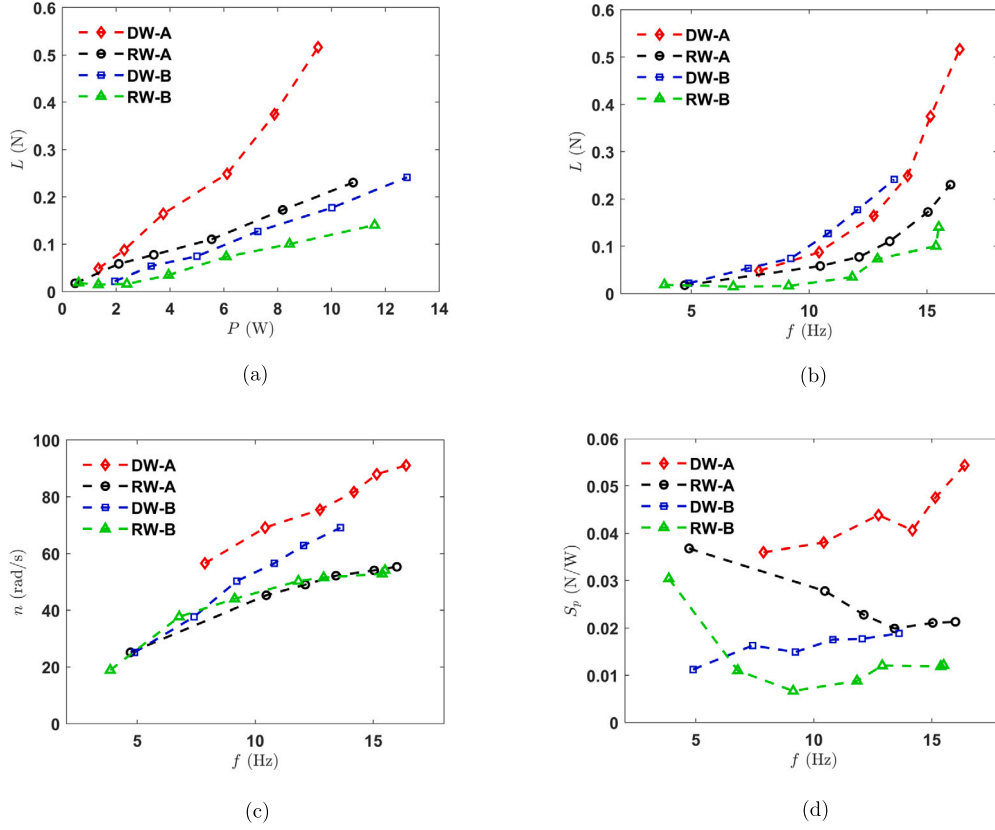
**Fig. 8.** The measured average lift force, input power, flapping frequency, rotation speed, and power efficiency of the FWR model with dragonfly-like wings and base wings: (a) the average lift against input power; (b) the average lift against flapping frequency; (c) rotation speed against flapping frequency; (d) power efficiency against flapping frequency.

**Table 2**
Measured and CFD results of Wing DW-A and Wing RW-A.

| Model | $P$ (W) | $L$ (N) | $S_P$ (N/W) | $f$ (Hz) | $n$ (rad/s) | $\bar{C}_l$ (test) | $\bar{C}_l$ (CFD) |
|---|---|---|---|---|---|---|---|
| Wing DW-A | 2.3 | 0.088 | 0.038 | 10.47 | 69 | 0.61 | 0.58 |
| Wing RW-A | 2.1 | 0.058 | 0.028 | 10.42 | 45 | 0.40 | 0.43 |

to a faster rotation speed (Fig. 8(c)). As the rotation speed of the DW wings rose significantly with flapping frequency to enhance lift generation, the power efficiency of the DW wings generally increased, whereas the power efficiency of the RW wings decreased with increasing flapping frequency (Fig. 8(d)).

Specifically, the cases of DW-A and RW-A wings at a frequency of approximately 10.5 Hz are detailed in Table 2. There are slight differences between the CFD model and experimental measurements: the CFD simulation value of the average lift coefficient has a difference of 4.99% compared to the measured difference in the Wing DW-A case and a difference of 6.65% in the Wing RW-A case. In the above results, using the Wing DW can increase the average lift by 50% and power by 36% when compared to the Wing RW-A. Furthermore, the faster rotational speed of Wing DW-A compared to Wing RW-A corresponds to an increase in the incoming flow velocity. Thus, the aerodynamic forces increase, and the effective angle of attack shifts. This is highlighted more prominently in the CFD results, as shown in Fig. 9, where the peak positive lift generates during the downstroke of Wing DW-A increases and the negative lift during the upstroke decreases. The peak rotation moment during the downstroke also increases significantly. The $\bar{C}_m$ values of Wing DW-A and Wing RW-A are 0.062 and 0.0577, respectively.

*3.1.2. Flow analysis*

The shape of the wing has a direct effect on the flow around the wing, i.e., the aerodynamic mechanism of the FWR wing, which consists

of an attached leading edge vortex (LEV), added mass, wake capture, and rotational circulation. Given that the quasi-steady model utilized in previous investigations did not incorporate the effects of spanwise flow and wingtip vortex, the CFD method is a suitable and precise method for elucidating the aerodynamic mechanism of dragonfly-like FWR wings through the visualization of flow fields around the wing.

The LEV has been identified as a major contributing factor to the high lift production for the insect flights [39–41]. The DW wing can generate high lift and have great aerodynamic efficiency, which is mainly because the LEV develops and extends to the wingtip along the curvature of the LE-beam and remains stably attached to the wing surface. This can be obviously seen in Fig. 10: when the spanwise velocity increases, the LEV core transports vorticity towards the wingtip, and the wingtip curvature of Wing DW-A allows the vorticity to smoothly extend to the tailing edge. The resulting vortex ring connects the leading edge and tailing edge (at $\hat{t} = 1.3$ in Fig. 10(a)). In contrast, the spanwise LEV of Wing RW-A sheds at the wingtip (at $\hat{t} = 1.245$ in Fig. 10(b)). Moreover, the greatest LEV development occurs on Wing DW-A when the lift coefficient reaches its maximum value at $\hat{t} = 1.3$, and the vortex formation is later than on Wing RW-A. For Wing RW-A, the vortex forms fully at $\hat{t} = 1.245$. The maximum vortex formation of Wing DW-A is also delayed in terms of the peak value of flapping velocity emerging at $\hat{t} = 1.25$, which is beneficial for enhancing lift production. Therefore, this sweep-back wingtip shape makes effective use of the stable attachment of the LEV and delayed stall mechanism.
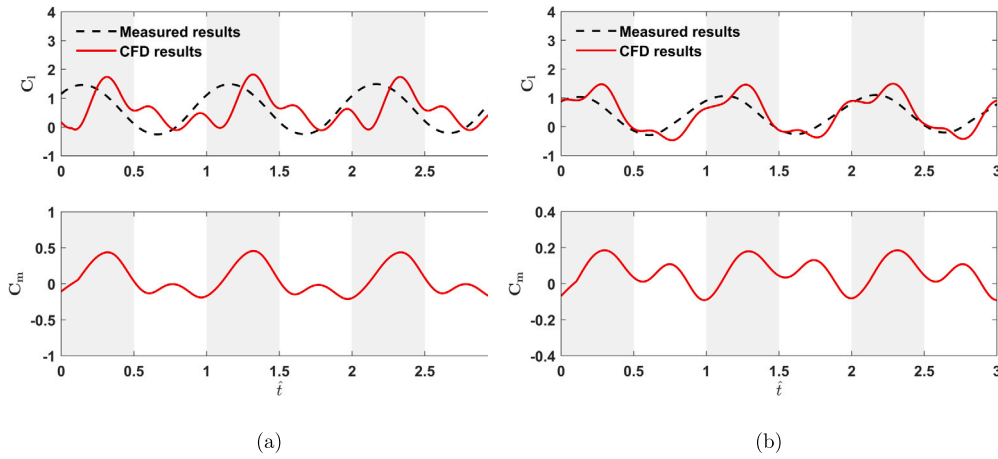
**Fig. 9.** Time course of lift and moment coefficients of (a) Wing DW-A and (b) Wing RW-A.
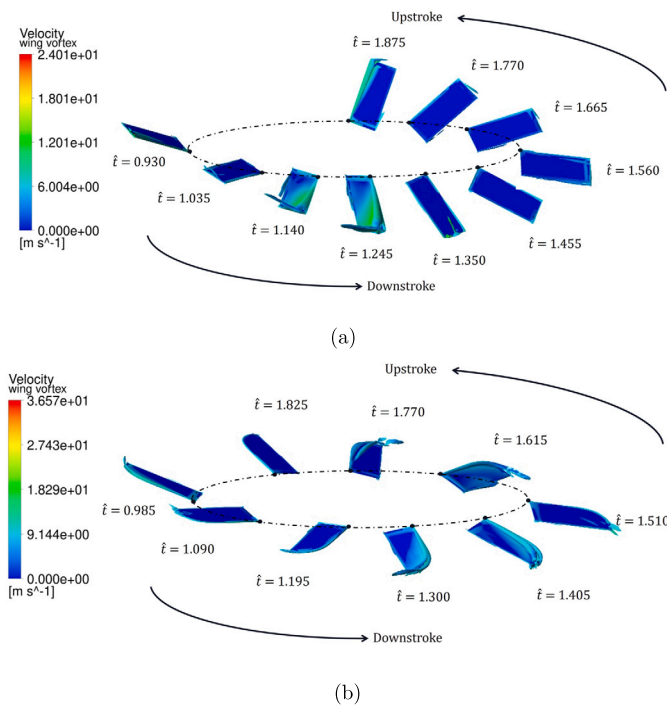


(a)

(b)

**Fig. 10.** Wing vorticity distribution of 10.5 Hz flapping examples with colour indication of velocity variation over a flapping cycle: (a) Wing DW-A and (b) Wing RW-A.

### 3.2. Effect of aspect ratio

Fig. 8 presents the experimental results of the DW and RW wings, which demonstrate the effect of aspect ratio on aerodynamic forces and power efficiency. Specifically, when comparing Wing DW-A ($\lambda = 2.67$) and Wing DW-B ($\lambda = 1.78$) at the same flapping frequency, the lower rotation speed of Wing DW-A compared to Wing DW-B with a small aspect ratio leads to a lift-to-drag ratio, hence a lower power efficiency.

Similar conclusions are drawn when comparing their rectangular baselines, Wing RW-A ($\lambda = 2.67$) and Wing RW-B ($\lambda = 1.78$), indicating that decreasing aspect ratio increases the wing's area and weight, leading to changes in passive pitching motion due to inertial forces and altering the direction of the effective angle of attack, resulting in decreased lift and increased thrust. Overall, the power efficiency deteriorates.
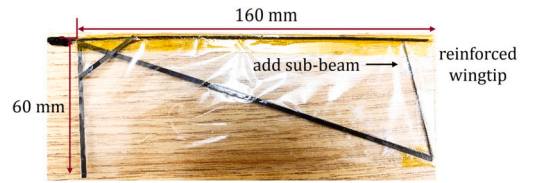


**Fig. 11.** Structure and dimensions of Wing RW-C.

**Table 3**
Dimensions and weight of Wing RW-C.

| Parameters | Wing RW-C |
|---|---|
| Dimension (mm) | 160×60 |
| $\lambda$ | 2.67 |
| Weight ($g$) | 0.85 |

### 3.3. Effect of wingtip chordwise stiffness

#### 3.3.1. Aerodynamic forces and power efficiency

The above Section 3.1 demonstrates that DW wings can generate greater lift than RW wings. This is not only due to the aerodynamic changes caused by the shape but also due to the factor of reinforced wingtip stiffness. The LE-beam of the DW wing encloses the wingtip, enhancing its chordwise stiffness. To analyse and verify the effect of this point, a sub-beam was added at the wingtip of Wing RW-A, as shown in Fig. 11. Wing RW-A is compared with the reinforced Wing RW-C under the same shape conditions. See Table 3.

The measured results of Wing RW-C in comparison to Wing RW-A are shown in Fig. 12. When compared under the same input power or frequency conditions, the reinforced Wing RW-C has greater lift than the original Wing RW-A (Fig. 12(a)(b)). The two wings have approximately the same rotational speed at the same flapping frequency (Fig. 12(c)). It can be inferred from the curves plotted in Fig. 12 that when the FWR model with Wing RW-C flaps at a frequency of 10.5 Hz, it generates a total average lift of 0.09 N, which is 1.55 times higher than that generated by Wing RW-A. Moreover, its input power is 2.9 W, and its power efficiency is 0.031 N/W, which is 1.11 times that of Wing RW-A (Fig. 12(d)). The above results imply that the presence of a reinforced wingtip in the FWR wing has a positive impact on lift generation enhancement, as opposed to thrust, at the specified flapping frequency.

#### 3.3.2. Dynamic responses

The reinforcement of the wingtip affects the deformation of the flexible wings in terms of twist and bend, which has a positive impact on lift production. Fig. 13 presents the results from the aerodynamic and
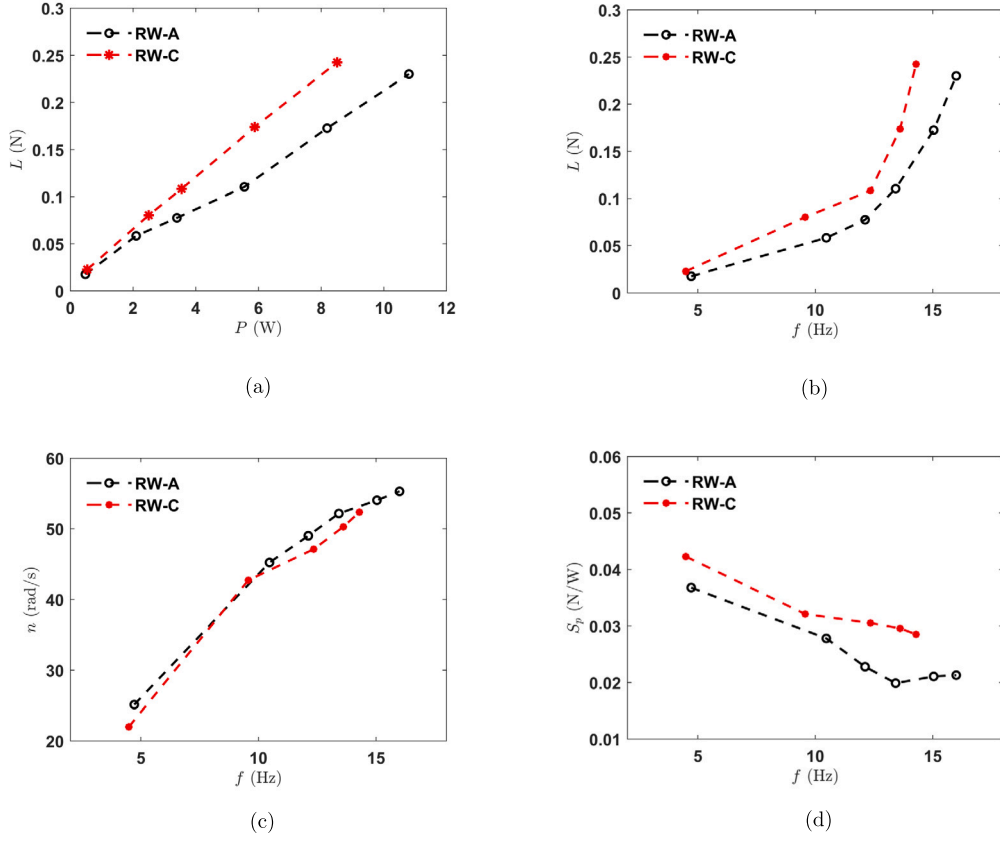
Fig. 12. The measured results of the FWR model with Wing RW-C compared with Wing RW-A: (a) the average lift against input power; (b) the average lift against flapping frequency; (c) rotation speed against flapping frequency; (d) power efficiency against flapping frequency.
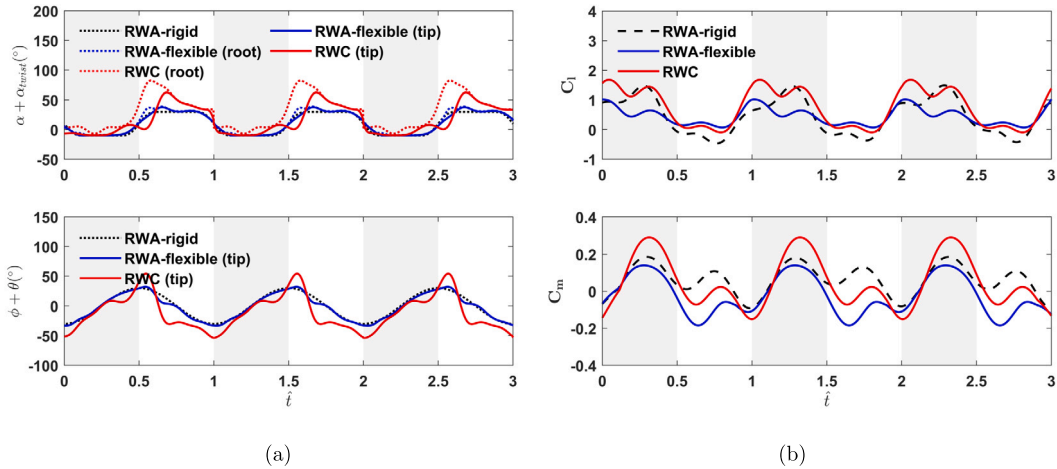


Fig. 13. Wing deflections and aerodynamic forces of Wing RW-A and reinforced Wing RW-C under the CFD/CSD simulations: (a) pitching and twisting angles of wing root and tip, flapping and bending angles of wingtip at the LE-beam; (b) time courses of lift and moment coefficients.

structural coupling simulations, showcasing the lift and moment coefficients, as well as the elastic deformations at the wing root and wingtip for both Wing RW-A and Wing RW-C, flapping at 10.5 Hz with a rotational speed of 45 rad/s. The twisting angle of Wing RW-C is greater than that of Wing RW-A due to the former's lump mass at the wingtip, which results in a higher passive twisting moment around the spanwise axis of the LE-beam. The centre of mass of Wing RW-C in the chordwise direction is located at $0.37\,\bar{c}$, while that of Wing RW-A is located at $0.34\,\bar{c}$, contributing to the difference in twisting angle. Moreover, the wingtip stiffness of Wing RW-C leads to a smaller peak twisting deformation at the wingtip compared to that at the wing root, which

is not observed in Wing RW-A. The lump mass also increases the spanwise bending of Wing RW-C, causing higher lift and rotation coefficients with $\bar{C}_l = 0.74$ and $\bar{C}_m = 0.048$ at larger flapping and pitching angles, while the flexible Wing RW-A model has lower values of $\bar{C}_l = 0.45$ and $\bar{C}_m = -0.024$, requiring more power. The above results indicate that the wing inertia plays a significant role in wing deformation and aerodynamic performance.

Fig. 14 further presents the initial effect of the wings during the downstroke and upstroke that result in rapid pitching and flapping variations in the flexible wing. During the initial state ($\hat{t}$ from 1.02 to 1.20), upward bending deformation allows Wing RW-C to exhibit large flap-
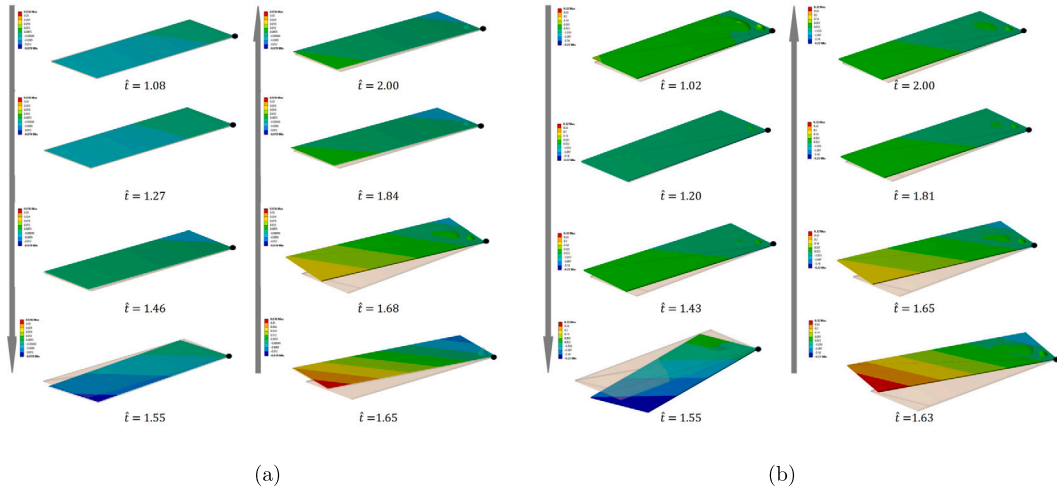
$\hat{t} = 1.08$    $\hat{t} = 2.00$    $\hat{t} = 1.02$    $\hat{t} = 2.00$

$\hat{t} = 1.27$    $\hat{t} = 1.84$    $\hat{t} = 1.20$    $\hat{t} = 1.81$

$\hat{t} = 1.46$    $\hat{t} = 1.68$    $\hat{t} = 1.43$    $\hat{t} = 1.65$

$\hat{t} = 1.55$    $\hat{t} = 1.65$    $\hat{t} = 1.55$    $\hat{t} = 1.63$

(a)      (b)

**Fig. 14.** Transient deformations in z-direction of flexible (a) Wing RW-A and (b) Wing RW-C (unit m).
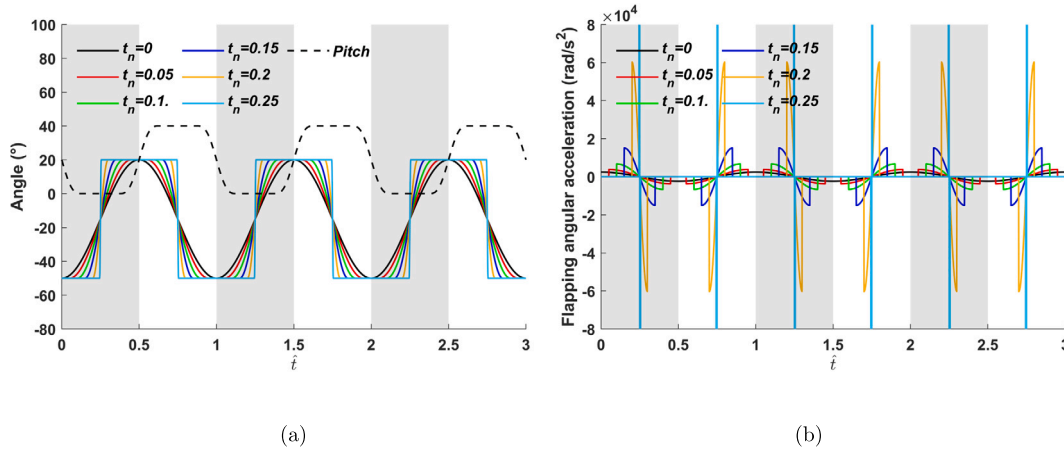


(a)      (b)

**Fig. 15.** Transient deformations in z-direction of flexible (a) Wing RW-A and (b) Wing RW-C.

ping angles with a peak value of lift (seen in Fig. 13(b)). The wing experiences serious deformations during the period between the end of the downstroke and the beginning of the upstroke ($\hat{t}$ from 1.43 to 1.65), including reverse flapping and pitching angles. This induces a delayed pitching angle variation at the wingtip compared to the wing root and rigid model, ultimately reducing thrust production.

Prior research of a pitching-flapping-perturbed revolving wing suggests that advanced pitching can enhance the reduction of external driving torque, while delayed pitching can decrease both the driving torque and lift production [42]. Furthermore, the lift of a flapping wing can increase from rapid pitch rotation about the spanwise axis prior to the end of the stroke, but if the wing rotates after approaching the end of the stroke as delayed pitching rotation, the lift is reduced [43,44]. Despite the decrease in thrust production caused by the elastic deformation of the wing during this flapping reversed period, the upward bending deflection during the upstroke can maintain lift generation. This demonstrates the significance of bending deflection in affecting the aerodynamic performance of the flexible wing.

### 3.4. Effect of spanwise stiffness and deformation

The thickness variation in dragonfly wings is a result of venation, where veins surround the membrane and gradually decrease in thickness from the wing root to the wingtip. This allows dragonflies to maintain unsteady flight with high efficiency. Therefore, the spanwise stiffness of the wings is particularly important for effectively controlling

wing deformation during flapping. This study focuses on investigating the mechanism of the spanwise deformation effect of the wings on the aerodynamic forces of FWR, with the aim of finding the best use of flexible wings for optimal performance inspired by the dragonfly wings.

#### 3.4.1. Aerodynamic mechanism of spanwise wing deformation

Similar to the advanced pitching rotation, it can be inferred that delaying the acceleration of flapping at the beginning or end of the stroke can improve lift and thrust generation. As demonstrated in Section 3.3.2 above, during the initial state of flapping downstroke and upstroke, a flexible wing undergoes a bending deformation, causing it to lag behind the rigid rotation during the stroke. Hence, the effect of spanwise deformation of the flexible wing on the aerodynamics can be considered as an effect of the delayed vortex formation resulting from the corresponding delay in flapping motion.

The flapping delay process is modelled as a time interval during which the flapping wing maintains a constant flapping angle at the beginning of the downstroke and upstroke. This time interval is denoted by a dimensionless flapping delay time ($t_n$), and its value divided by the flapping frequency yields the physical time of flapping delay. In this study, the wing motion is simulated with flapping amplitudes of 70°, pitching amplitudes of 40°, and a rotation speed of 8.2 rad/s, as shown in Fig. 15(a). At a flapping frequency of 10 Hz, different flapping delay time ($t_n$) cases are considered. The $t_n = 0$ case represents non-delayed flapping with rigid rotation. Increasing $t_n$ causes a back-

**Table 4**
Cases for modelling the FWR wing with flexibility along the spanwise.

| Cases | Node (r/R) | 0 | 0.2 | 0.4 | 0.6 | 0.8 | 1 | Flexibility |
|-------|------------|---|-----|-----|-----|-----|---|-------------|
| Rigid | $t_n$ | 0 | 0 | 0 | 0 | 0 | 0 | stiff |
| FW-A | $t_n$ | 0 | 0 | 0 | 0.005 | 0.02 | 0.05 | |
| FW-B | $t_n$ | 0 | 0 | 0.005 | 0.02 | 0.05 | 0.1 | |
| FW-C | $t_n$ | 0 | 0.005 | 0.02 | 0.05 | 0.1 | 0.15 | |
| FW-D | $t_n$ | 0 | 0.02 | 0.05 | 0.1 | 0.15 | 0.2 | |
| FW-E | $t_n$ | 0 | 0.05 | 0.1 | 0.15 | 0.2 | 0.25 | flexible |



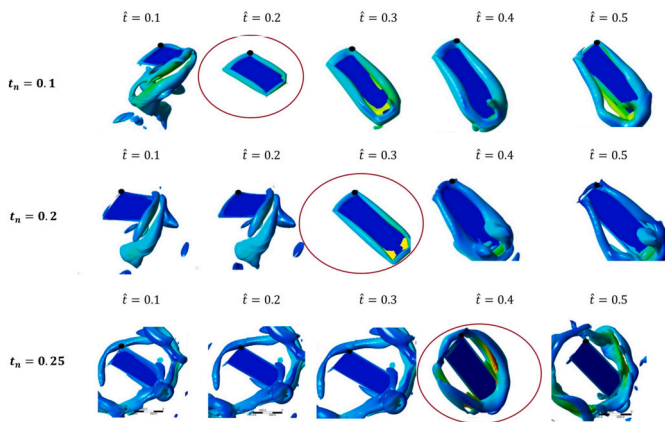**Fig. 16.** The simplified wing model of Wing DW-A.



**Fig. 17.** Vorticity variation of the wing model during the downstroke in different delayed flapping cases at a flapping frequency of 10 Hz.

ward delay in the occurrence of the peak of acceleration, as shown in Fig. 15(b).

To streamline the calculations, a simplified rigid wing model based on the shape of the Wing DW-A was taken in CFD simulations, as depicted in Fig. 16. This model exhibits consistent flow characteristics with the Wing DW-A. The sweep-back wingtip shape can promote the extension of the leading-edge vortex and the formation of a vortex ring attached to the wing surface, which is conducive to high lift production, as shown in Fig. 17. It is also demonstrated that delayed flapping motion affects vortex formation during the downstroke. The formation of vortices in cases $t_n = 0.1$ and $t_n = 0.2$ occurs at $\hat{t} = 0.2$ and $\hat{t} = 0.3$ respectively, corresponding to the wing's downward motion with a high flapping velocity. The maximum lift generated occurs when a stable and complete vortex ring attaches to the wing surface. However, for $t_n = 0.25$, the extremely rapid flapping rotation at the end of stroke, coupled with poor synchronization between flapping and pitching motions, results in the vortex detaching from the wing surface during a flapping cycle, leading to undesirable aerodynamic performance. Further details on the aerodynamic forces are presented in the following Fig. 18.

Fig. 18(a) shows the instantaneous lift coefficient of the wing model at 10 Hz with the same delay flapping $t_n$ from the wing root to the wingtip. The peak of lift coefficient increases significantly around the mid-stroke with an increase of $t_n$ from 0 to 0.25, owing to the corresponding increase in flapping velocity and acceleration. Therefore, the wing model benefits from delayed flapping time, exhibiting a higher

mean lift coefficient than the non-delayed case $t_n = 0$. Fig. 18(b) reveals that the maximum lift coefficient generated by delayed flapping $t_n = 0.2$ increases by 71%, 69%, 91%, and 96% at 5 Hz, 10 Hz, 15 Hz, and 20 Hz, respectively, compared to the non-delayed case. However, when the flapping motion is significantly delayed to $t_n = 0.25$, the lift coefficient experiences a sharp decline due to the negative lift force generated during the upstroke.

The effect of delayed flapping on thrust (negative drag) is shown in Fig. 18(c), where a decrease followed by a gradual increase in thrust is observed at low frequencies of 5 Hz and 10 Hz. During this frequency range, high lift production leads to a corresponding increase in aerodynamic power efficiency $P_f$, as demonstrated in Fig. 18(d), compared to the non-delayed case. In contrast, thrust continues to increase with the flapping frequency beyond 15 Hz. However, when the delayed time $t_n$ exceeds 0.2, although thrust reaches high values, the aerodynamic power efficiency drops dramatically below zero due to the negative average lift. Overall, the above results indicate that the wing loses its function if it is too flexible to cause a large delay in flapping, i.e., $t_n > 0.2$.

### 3.4.2. Effect of wing flexibility

According to the above analysis, the spanwise deformation of the flapping wing affects the aerodynamic forces through the vortex delay mechanism. The wing deformation can be modelled as the bending of a cantilever beam, with varying flapping delay time $t_n$ along the spanwise direction. The nodes along the spanwise direction are denoted by $r$, with $t_n$ increasing gradually from the wing root to the wingtip, as tabulated in Table 4. In this analysis, the wing model without delayed flapping serves as a rigid baseline. The cases FW-A to FW-E represent the increasing flexibility of the wing. A node represents a chordwise wing strip, and the segment's aerodynamic forces are determined by the wing's rotational speed at that location and the corresponding aerodynamic coefficients obtained for each delayed flapping time. These forces are then integrated along the entire wing to obtain the total force.

The aerodynamic performance of the wings from FW-A to FW-E, is presented in Fig. 19. Except for the FW-E, which has the greatest flexibility in deforming from the wing root, all other wings can achieve better aerodynamic performance than the rigid baseline wing.

It is also interesting to find that FW-E produces the highest thrust but negative average lift. Among the these wing models, FW-D exhibits the highest performance, with a lift enhancement of 58% to 68% compared to the rigid wing flapping at a frequency between 10 Hz and 20 Hz. However, its power efficiency diminishes and becomes lower than the rigid wing after 15 Hz. FW-C also exhibits lower power efficiency than that of the rigid wing at 15 Hz. In contrast, FW-B increases the lift by 38% to 47% at a frequency range between 10 Hz and 20 Hz, with the maximum power efficiency at 10 Hz and keeping it higher than the rigid wing until 15 Hz. According to the study, the deformation pattern of FW-B is most suitable in general performance for the FWR, flapping frequencies.

### 3.4.3. Variable spanwise stiffness

By disregarding the twisting deformation, the deflection of the wing in the spanwise direction is calculated through the utilization of the cantilever beam equation, expressed as follows:
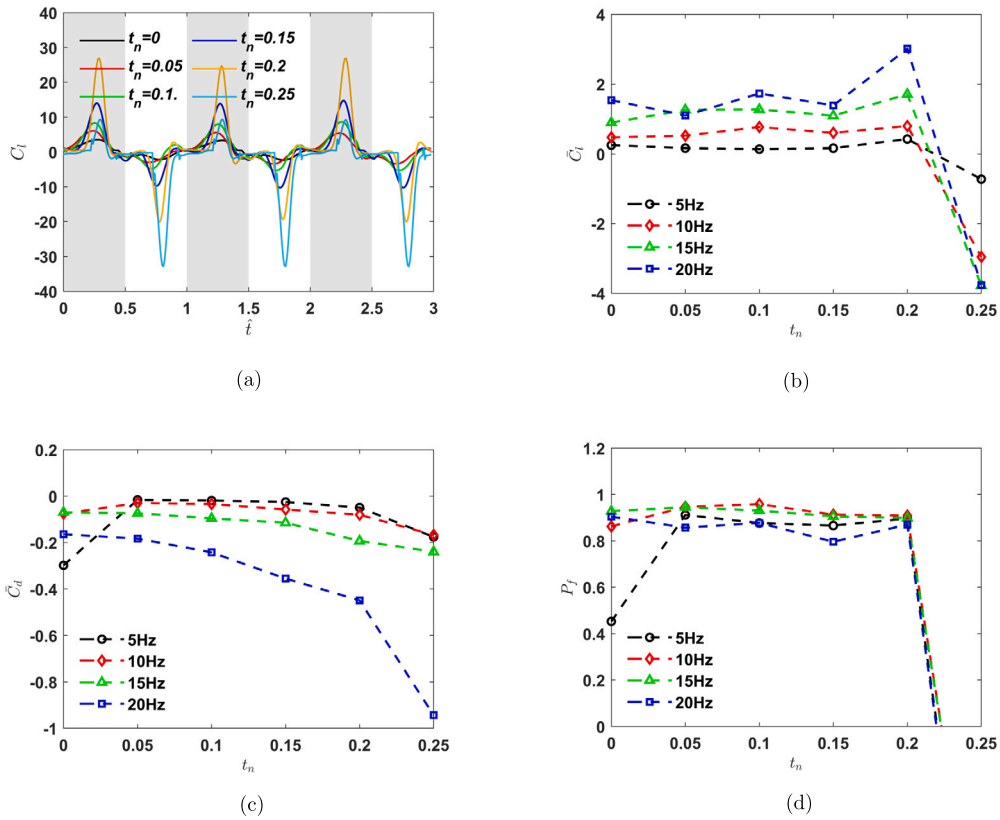
(a)

(b)

(c)

(d)

**Fig. 18.** (a) Time course of lift coefficient of the wing model at the flapping frequency of 10 Hz; Variations of (b) the mean lift coefficient, (c) the mean thrust coefficient, and (d) the aerodynamic power efficiency (d) against the different flapping delay times at the flapping frequencies of 5 Hz, 10 Hz, 15 Hz, and 20 Hz.
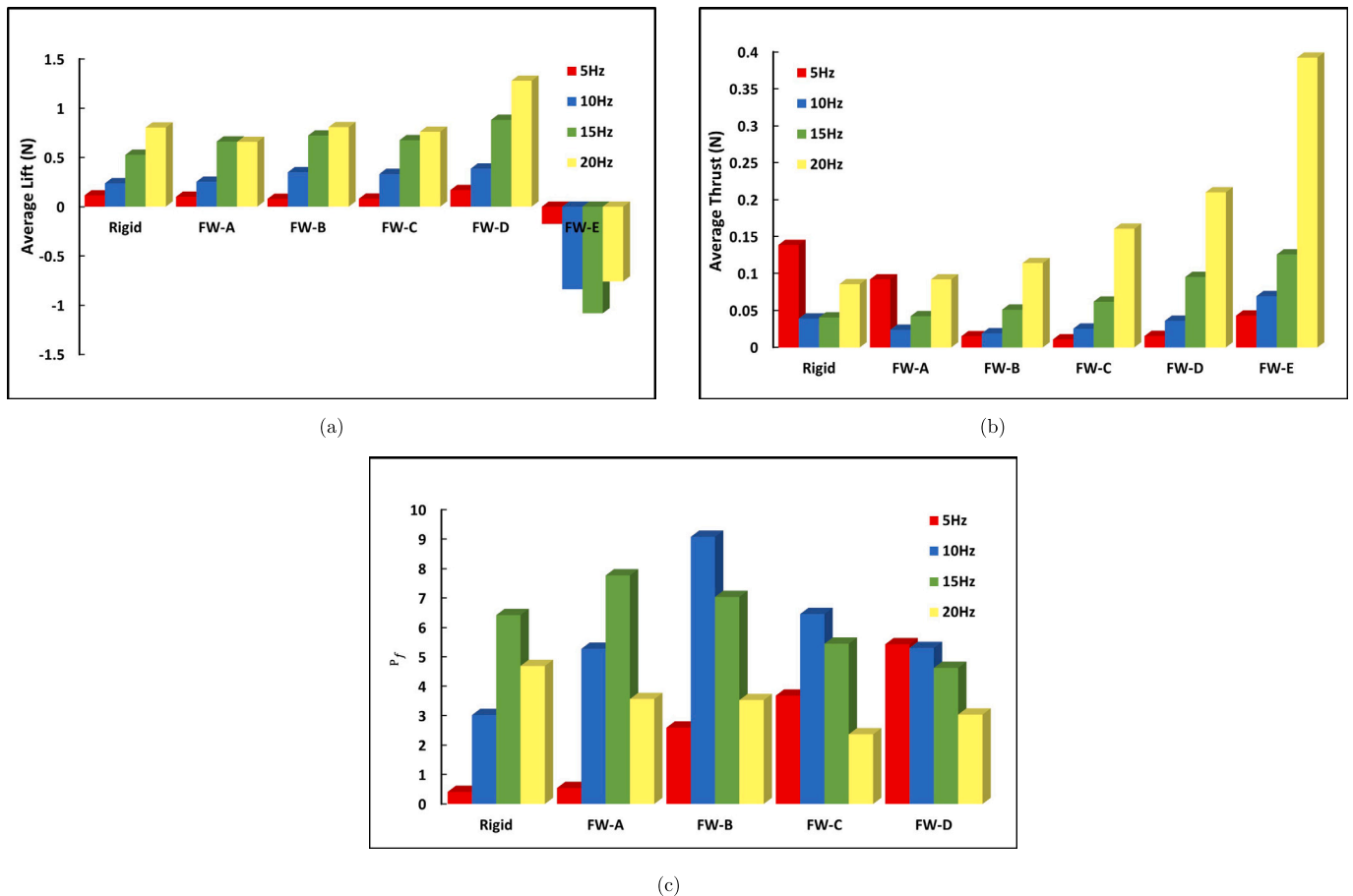


(a)

(b)

(c)

**Fig. 19.** (a) Average lift, (b) average thrust, and (c) power efficiency of the modelled flexible wing (from FW-A to FW-E) in a flapping cycle.
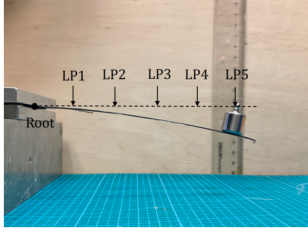
**Fig. 20.** Schematic of wingspan stiffness static measurement.

$$EI \cdot z_w(r) = \int_{r=0}^{R} \left[ \int_{r=0}^{R} -M_y(r)dr \right] dr \qquad (12)$$

where the vertical deflection $z_w(r)$ is determined based on the reference flapping velocity at $r$ and the physical delayed time ($t_n/f$), i.e., $z_w(r) = U_{ref}(r) \bullet t_n/f$; $EI$ indicates the spanwise stiffness of the flexible wing model; the bending moment endured by the wing $M_y$ is computed by integrating the sectional lift force along the span.

The $EI$ of a physical FWR wing is measured by placing a lumped mass on the LE-beam along various spanwise positions (LP1 to LP5), as illustrated in Fig. 20. By measuring the vertical displacement of the wing at each loading point and applying the cantilever beam deflection equation (12), the $EI$ of the wing cross-section is determined.

Fig. 21(a) illustrates that under the 10 Hz flapping motion condition, the most flexible FW-D model produces the largest deflection at the wingtip (0.077 m) with a flapping delay of $t_n = 0.2$. On the other hand, the relatively stiffer FW-A exhibits the smallest deflection (0.019 m) with a flapping delay of $t_n = 0.05$. The $EI$ values obtained from these deflection calculations are compared with the measured stiffness of the wing test models (DW-A, RW-A, and RW-C) in Fig. 21(b).

Among the test models, the Wing RW-A has the smallest stiffness, similar to FW-D. As a result, the delayed mechanism cannot be fully utilized, leading to poor aerodynamic efficiency. After wingtip reinforcement, the spanwise stiffness of the Wing RW-C is between FW-C and FW-D, resulting in improved lift and power efficiency. In contrast, the stiffness of the Wing DW-A varies along the spanwise direction in a pattern between FW-B and FW-A, exhibiting significant delayed vortex generation effects. Therefore, the Wing DW-A exhibits the highest aerodynamic efficiency among the other test wing models.

These results indicate that excessive flexibility can lead to increased elastic deformation, impeding vortex formation and stability, and decreasing aerodynamic efficiency. Within the range of stiffness evaluated in this study, i.e., from FW-A to FW-D, moderate flexibility with spanwise stiffness variation resulting in elastic deformation that delays wing flapping motion from the wing's middle to the wingtip (flapping delay of $t_n = 0.1$) can achieve the greatest aerodynamic efficiency for flexible wings. Additionally, the dragonfly-like wing model presented in this

study can be easily constructed by adjusting the thickness of the curving LE-beam, enabling the FWR-MAV to obtain aerodynamic benefits from a flexible structure.

### 3.5. Flight test of the FWR-MAV with dragonfly-like wings

The FWR model (Fig. 2) driven by a DC motor was built with a total weight of 25 g, including a 3.7 V lithium battery and flight control board. Experimental measurements in Fig. 8(a) demonstrated that with a 3.5 V DC supply input, the FWR model using the Wing DW-A generated sufficient lift (38 g at 7.88 W) to take-off, while the rectangular wing model (Wing RW-A) produced only 17.6 g (8.2 W) of lift. Consequently, the FWR model equipped with Wing DW-A successfully achieved vertical take-off and hovering in both indoor and outdoor tests by remote control, as illustrated in Fig. 22(a)(b)(c). The FWR-MAV model was able to take 2 s to take off at the maximum throttle and kept hovering in the air for 3 s. The remote control adjusts motor input power to alter flapping frequency without attitude control, showcasing the FWR-MAV model's self-stabilization capability during free flights.

Furthermore, owing to the high lift production and power efficiency of dragonfly-like wings, the FWR model, employing the same pair of wings and driven by two motors, increased the take-off weight to 51 g and successfully completed flights, as shown in Fig. 22(d). Due to the significantly higher lift coefficient, the FWR has a clearly larger take-off weight-to-wingspan ratio than most conventional insect-like flapping wing MAVs. For example, using a single motor configuration, the 19 g Nano Hummingbird [45] has a wingspan of 165 mm, while the 22 g Colibri [46] has a wingspan of 210 mm. The dual-motor butterfly-type ornithopter has a weight of 38.6 g and extends the wingspan to 648 mm [47]. In future research, the flight control system, encompassing attitude mechanisms, will be explored to achieve stable VTOL, hovering, and forward flights for practical FWR-MAV applications.

### 4. Conclusion

This study examined the aerodynamic performance of a flexible wing for flapping wing rotors, focusing on the beneficial effects of wing stiffness and a sweep-back wingtip shape on high lift and power efficiency. The investigation involved a multi-faceted approach, encompassing design, numerical analysis, manufacturing, and experimentation of FWR wing models to compare with baseline rectangular wings. CFD analysis revealed the significant benefit of the sweep-back wingtip shape and the underlying aerodynamic mechanism, particularly the formation of the LE/TE vortex ring and vortex delay. Experimental results of the wing models validate the numerical models and analysis. By adapting a backward-curved wingtip, the lift can be increased by 50%.

The FSI analysis was employed to evaluate the effect of the reinforced wingtip structure. By comparing the baseline rectangular wings
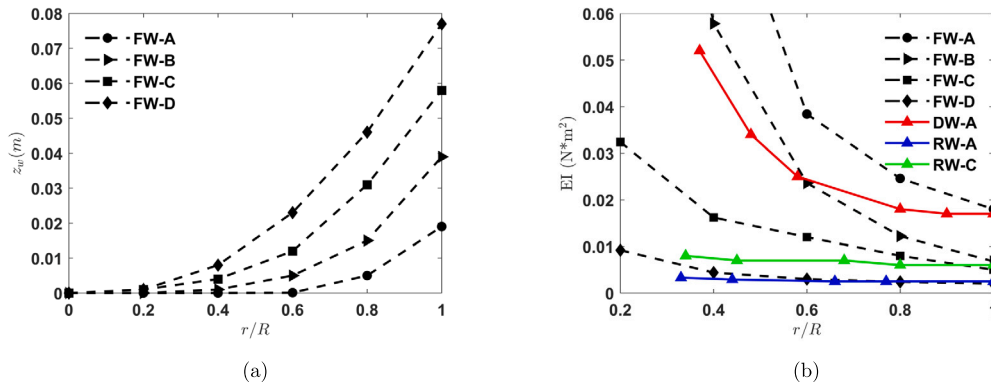




(a)                    (b)

**Fig. 21.** (a) Average deflection over a flapping cycle along the wingspan at 10 Hz flapping frequency and (b) comparison of the equivalent stiffness of flexible wing models (FW-A to FW-D) and the measured stiffness of the wing test models (DW-A, RW-A and RW-C).

**Fig. 22.** Single-motor FWR-MAV model with dragonfly-like wings: (a) free launch from hand; (b) vertical take-off in indoor test; (c) outdoor test; (d) Dual-motor FWR-MAV model out door test.

with and without enhanced stiffness at the wingtip, the results of numerical simulations and experiments showed that the reinforced wingtip is beneficial for lift enhancement due to the enlarged pitching and flapping angles.

The investigation further revealed that the mechanism of bending deformation enhances lift and power efficiency in FWR wings. The vortex delay mechanism was found to be associated with wing bending deformation through delayed flapping motion. The analysis was validated by comparing spanwise stiffness to the measured stiffness of the FWR wings. The study found that a certain spanwise flexibility can cause a small delayed flapping motion and improve aerodynamic performance. The present results show that the lift can be increased by 58% to 68%. The curving LE-beam forming the sweep-back wingtip, which can be conveniently adjusted for thickness, provides a way to achieve variable stiffness and aerodynamic advantages for FWR-MAVs. By employing the designed dragonfly-like wings, the FWR model demonstrated high lift production and power efficiency across multiple flight tests. These findings contribute valuable insights for developing more efficient and agile flexible wings for FWR-MAVs.

**Declaration of competing interest**

The authors declare that they have no known competing financial interests or personal relationships that could have appeared to influence the work reported in this paper.

**Data availability**

No data was used for the research described in the article.

## References

[1] H.V. Phan, H.C. Park, Insect-inspired, tailless, hover-capable flapping-wing robots: recent progress, challenges, and future directions, Prog. Aerosp. Sci. 111 (March) (2019) 100573, https://doi.org/10.1016/j.paerosci.2019.100573.

[2] L. Petricca, P. Ohlckers, C. Grinde, Micro- and nano-air vehicles: state of the art, Int. J. Aerosp. Eng. (2011), https://doi.org/10.1155/2011/214549.

[3] D.D. Chin, D. Lentink, Flapping wing aerodynamics: from insects to vertebrates, J. Exp. Biol. 219 (7) (2016) 920–932, https://doi.org/10.1242/jeb.042317.

[4] H. Li, S. Guo, Y.L. Zhang, C. Zhou, J.H. Wu, Unsteady aerodynamic and optimal kinematic analysis of a micro flapping wing rotor, Aerosp. Sci. Technol. 63 (April) (2017) 167–178, https://doi.org/10.1016/j.ast.2016.12.025.

[5] H. Li, Aeroelastic investigation of conventional fixed wings and bio-inspired flapping wings by analysis and experiment, Ph.D. thesis, Cranfield, 2018.

[6] D. Li, S. Guo, N. Di Matteo, D. Yang, Design, experiment and aerodynamic calculation of a flapping wing rotor micro aerial vehicle, in: Collect. Tech. Pap. - AIAA/ASME/ASCE/AHS/ASC Struct. Struct. Dyn. Mater. Conf. (April), 2011, pp. 1–9.

[7] S. Guo, H. Li, C. Zhou, Y.L. Zhang, Y. He, J.H. Wu, Analysis and experiment of a bio-inspired flyable micro flapping wing rotor, Aerosp. Sci. Technol. 79 (2018) 506–517, https://doi.org/10.1016/j.ast.2018.06.009.

[8] S. Chen, L. Wang, Y. He, M. Tong, Y. Pan, B. Ji, S. Guo, Aerodynamic performance of a flyable flapping wing rotor with passive pitching angle variation, IEEE Trans. Ind. Electron. PP (2021) 1, https://doi.org/10.1109/TIE.2021.3112964.

[9] X. Dong, Z. Wang, F. Liu, S. Li, F. Fei, D. Li, Z. Tu, Visual-inertial cross fusion: a fast and accurate state estimation framework for micro flapping wing rotors, 2022, pp. 1–18.

[10] D. Wang, J. Wu, Y. Zhang, Effects of geometric parameters on flapping rotary wings at low Reynolds numbers, AIAA J. 56 (4) (2018) 1372–1387, https://doi.org/10.2514/1.J055994.

[11] R. Wootton, The geometry and mechanics of insect wing deformations in flight: a modelling approach, Insects 11 (7) (2020) 1–19, https://doi.org/10.3390/insects11070446.

[12] H.V. Phan, H.C. Park, Wing inertia as a cause of aerodynamically uneconomical flight with high angles of attack in hovering insects, J. Exp. Biol. 221 (19) (2018), https://doi.org/10.1242/jeb.187369.

[13] M. Vanella, T. Fitzgerald, S. Preidikman, E. Balaras, B. Balachandran, Influence of flexibility on the aerodynamic performance of a hovering wing, 2009, pp. 95–105.

[14] J. Young, Details of insect wing design and deformation enhance aerodynamic function and flight efficiency, Science 1549 (2009), https://doi.org/10.1126/science.1175928.

[15] A. Shahzad, F.B. Tian, J. Young, J.C. Lai, Effects of flexibility on the hovering performance of flapping wings with different shapes and aspect ratios, J. Fluids Struct. 81 (2018) 69–96, https://doi.org/10.1016/j.jfluidstructs.2018.04.019.

[16] A. Evandro, Liani Shijun, Guo Giuliano, Aeroelastic effect on flapping wing performance, in: 48th AIAA/ASME/ASCE/AHS/ASC Struct. Struct. Dyn. Mater. Conf., vol. 2412, 2007.

[17] P. Wu, P. Ifju, B. Stanford, E. Sällström, L. Ukeiley, R. Love, R. Lind, A multidisciplinary experimental study of flapping wing aeroelasticity in thrust production (May), 2009, pp. 1–19.

[18] S. Heathcote, I. Gursul, Flexible flapping airfoil propulsion at low Reynolds numbers, AIAA J. 45 (5) (2007) 1066–1079, https://doi.org/10.2514/1.25431.

[19] L. Chen, F.L. Yang, Y.Q. Wang, Analysis of nonlinear aerodynamic performance and passive deformation of a flexible flapping wing in hover flight, J. Fluids Struct. 108 (3) (2022) 103458, https://doi.org/10.1016/j.jfluidstructs.2021.103458.

[20] S. Heathcote, Z. Wang, I. Gursul, Effect of spanwise flexibility on flapping wing propulsion, J. Fluids Struct. 24 (2) (2008) 183–199, https://doi.org/10.1016/j.jfluidstructs.2007.08.003.

[21] W. Yang, J. Xu, J. Xuan, Experimental study on the stiffness and shape layout of flapping wing, IOP Conf. Ser., Mater. Sci. Eng. 686 (1) (2019), https://doi.org/10.1088/1757-899X/686/1/012029.

[22] Y. Nan, M. Karásek, M.E. Lalami, A. Preumont, Experimental optimization of wing shape for a hummingbird-like flapping wing micro air vehicle, Bioinspir. Biomim. 12 (2) (2017) 026010, 2111–2122, 10.1088/1748-3190/aa5c9e.

[23] P. Wu, P. Ifju, B. Stanford, Flapping wing structural deformation and thrust correlation study with flexible membrane wings, AIAA J. 48 (9) (2010) 2111–2122, https://doi.org/10.2514/1.J050310.

[24] N. Phillips, K. Knowles, R.J. Bomphrey, The effect of aspect ratio on the leading-edge vortex over an insect-like flapping wing, Bioinspir. Biomim. 10 (5) (2015) 56020, https://doi.org/10.1088/1748-3190/10/5/056020.

[25] J.D. Eldredge, J. Toomey, A. Medina, On the roles of chord-wise flexibility in a flapping wing with hovering kinematics, J. Fluid Mech. 659 (2010) 94–115, https://doi.org/10.1017/S0022112010002363.

[26] A. Shahzad, F.B. Tian, J. Young, J.C. Lai, Effects of wing shape, aspect ratio and deviation angle on aerodynamic performance of flapping wings in hover, Phys. Fluids 28 (11) (2016), https://doi.org/10.1063/1.4964928.

[27] L. Zhao, X. Deng, Power distribution in the hovering flight of the hawk moth manduca sexta, Bioinspir. Biomim. 4 (4) (2009), https://doi.org/10.1088/1748-3182/4/4/046003.

[28] Q. Wang, J.F.L. Goosen, F.V. Keulen, An efficient fluid – structure interaction model for optimizing twistable flapping wings, J. Fluids Struct. 73 (2017) 82–99, https://doi.org/10.1016/j.jfluidstructs.2017.06.006.

[29] R. Godoy-Diana, B. Thiria, On the diverse roles of fluid dynamic drag in animal swimming and flying, J. R. Soc. Interface 15 (139) (2018), https://doi.org/10.1098/rsif.2017.0715.

[30] T. Nakata, H. Liu, Aerodynamic performance of a hovering hawkmoth with flexible wings: a computational approach, Proc. R. Soc. Lond. B, Biol. Sci. 279 (1729) (2012) 722–731, https://doi.org/10.1098/rspb.2011.1023.

[31] R. Kamakoti, W. Shyy, Fluid-structure interaction for aeroelastic applications, Prog. Aerosp. Sci. 40 (8) (2004) 535–558, https://doi.org/10.1016/j.paerosci.2005.01.001.

[32] R.J. Bomphrey, T. Nakata, P. Henningsson, H.T. Lin, Flight of the dragonflies and damselflies, Philos. Trans. R. Soc. Lond. B, Biol. Sci. 371 (1704) (2016), https://doi.org/10.1098/rstb.2015.0389.

[33] E. Salami, E. Montazer, T.A. Ward, N.N. Nik Ghazali, I. Anjum Badruddin, Aerodynamic performance of a dragonfly-inspired tandem wing system for a biomimetic micro air vehicle, Front. Bioeng. Biotechnol. 10 (May) (2022) 1–12, https://doi.org/10.3389/fbioe.2022.787220.

[34] H. Li, S. Guo, Aerodynamic efficiency of a bioinspired flapping wing rotor at low Reynolds number, R. Soc. Open Sci. 5 (3) (2018), https://doi.org/10.1098/rsos.171307.

[35] W. Jianghao, Z. Chao, Z. Yanlai, Aerodynamic power efficiency comparison of various micro-air-vehicle layouts in hovering flight, AIAA J. 55 (4) (2016) 1265–1278, https://doi.org/10.2514/1.J055221.

[36] K.O. Granlund, M.V. Ol, L.P. Bernal, Unsteady pitching flat plates, J. Fluid Mech. 733 (2013) 1–13, https://doi.org/10.1017/jfm.2013.444.

[37] K. Ramesh, A. Gopalarathnam, J.R. Edwards, M.V. Ol, K. Granlund, An unsteady airfoil theory applied to pitching motions validated against experiment and computation, Theor. Comput. Fluid Dyn. 27 (6) (2013) 843–864, https://doi.org/10.1007/s00162-012-0292-8.

[38] S. Chen, L. Wang, S. Guo, C. Zhao, M. Tong, A bio-inspired flappingwing rotor of variant frequency driven by ultrasonic motor, Appl. Sci. 10 (1) (2020) 1–21, https://doi.org/10.3390/app10010412.

[39] K.B. Lua, Y.J. Lee, T.T. Lim, K.S. Yeo, Aerodynamic effects of elevating motion on hovering rigid hawkmothlike wings, AIAA J. 54 (8) (2016) 2247–2264, https://doi.org/10.2514/1.J054326.

[40] A.L.R. Ellington, C.P. Van den Berg, C. Willmott, A.P. Thomas, Leading-edge vortices in insect flight, Nature 384 (1996) 356–358.

[41] Z.J. Wang, J.M. Birch, M.H. Dickinson, Unsteady forces and flows in low Reynolds number hovering flight: two-dimensional computations vs robotic wing experiments, J. Exp. Biol. 207 (3) (2004) 449–460, https://doi.org/10.1242/jeb.00739.

[42] L. Chen, J. Wu, C. Zhou, S.J. Hsu, B. Cheng, Unsteady aerodynamics of a pitching-flapping-perturbed revolving wing at low Reynolds number, Phys. Fluids 30 (5) (2018), https://doi.org/10.1063/1.5024925.

[43] M.H. Dickinson, F.O. Lehmann, S.P. Sane, Wing rotation and the aerodynamic basis of insect right, Science 284 (5422) (1999) 1954–1960, https://doi.org/10.1126/science.284.5422.1954.

[44] S.P. Sane, M.H. Dickinson, The aerodynamic effects of wing rotation and a revised quasi-steady model of flapping flight, J. Exp. Biol. 205 (8) (2002) 1087–1096, https://doi.org/10.1242/jeb.205.8.1087.

[45] M. Keennon, K. Klingebiel, H. Won, A. Andriukov, Development of the nano hummingbird: a tailless flapping wing micro air vehicle, AIAA J. (January) (2012) 1–24.

[46] A. Roshanbin, H. Altartouri, M. Karásek, A. Preumont, COLIBRI: a hovering flapping twin-wing robot, Int. J. Micro Air Veh. 9 (4) (2017) 270–282, https://doi.org/10.1177/1756829317695563.

[47] F. Leys, D. Vandepitte, D. Reynaerts, Design of a flapping wing micro air vehicle, based on the Rufous Hummingbird, in: 2015 IEEE Int. Conf. Robot. Biomimetics, IEEE-ROBIO 2015, 2015, pp. 1266–1271.

2024-03-29

# Aerodynamic performance of a flyable flapping wing rotor with dragonfly-like flexible wings

Pan, Yingjun

Elsevier